Check for updates

Synthetic helical dichroism for six-dimensional optical orbital angular momentum multiplexing

Xu Ouyang[1,2,9], Yi Xu [2,8,9], Mincong Xian[2], Ziwei Feng[1], Linwei Zhu [3], Yaoyu Cao[1], Sheng Lan [4], Bai-Ou Guan [1], Cheng-Wei Qiu [5], Min Gu [6,7✉] and Xiangping Li [1✉]

Optical multiplexing[1-11] by creating orthogonal data channels has offered an unparalleled approach for information encoding with substantially improved density and security. Despite the fact that the orbital angular momentum (OAM) of light involves physical orthogonal division, the lack of explicit OAM sensitivity at the nanoscale prevents this feature from realizing nanophotonic information encoding. Here we demonstrate the viability of nanoscale information multiplexing utilizing the OAM of light. This is achieved by discovering OAM-dependent polarization ellipses in non-paraxial focusing conditions and hence synthetic helical dichroism resulting from the distinct absorption of achiral nanoparticles to the different order of OAM beams. Leveraging this mechanism, the application of subwavelength-scale focused OAM beams to self-assemble plasmonic nanoaggregates further enables six-dimensional optical information multiplexing, in conjunction with wavelength, polarization and three spatial dimensions. Our results suggest the possibility of multiplexing OAM division as an unbounded degree of freedom for nanophotonic information encoding, security imprinting and beyond.
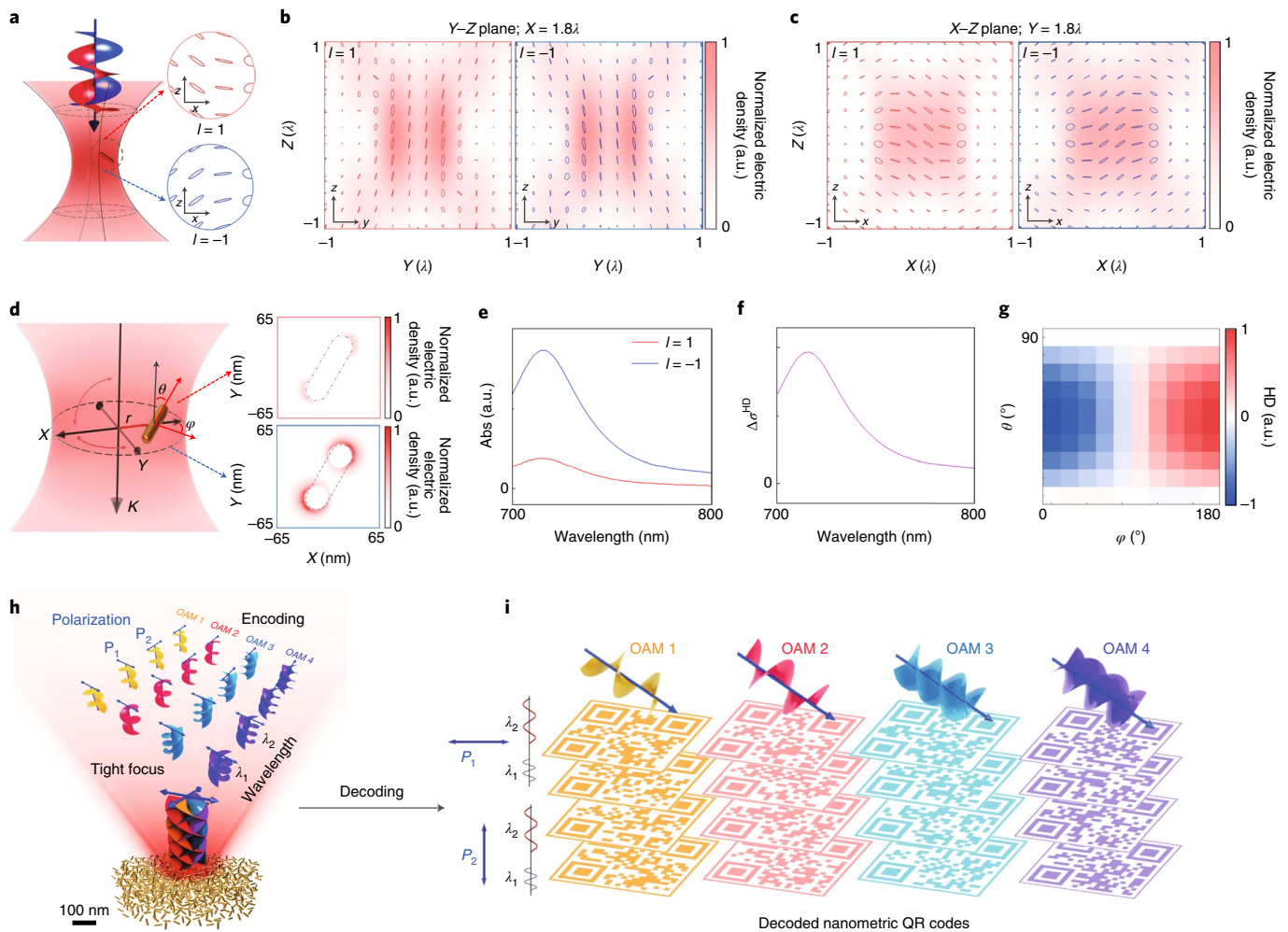
By creating orthogonal data channels among multiple attributes of light, such as in three-dimensional (3D) space[1,2], polarization[3-5], frequency[6,7], amplitude[8,9] and lifetime[10,11], optical multiplexing has become an indispensable tool for modern information technologies with orders of magnitude enhanced information density and security. The compelling demands for higher information capacity and higher security have further motivated intense research on confining light–matter interactions to the subwavelength scale by a variety of nanophotonic approaches[12] and exploiting exotic multidimensional light–matter interactions in new dimensions[1-11]. Having almost exhausted existing physical dimensions to multiplex information, optical encoding is rapidly approaching its limit. Therefore, exploring the orbital angular momentum (OAM) of light has recently emerged as a new opportunity.

Since it was first theoretically conceived[13] and experimentally demonstrated[14,15] that light can carry OAM, manifested by its helical phase wavefront of $\exp(i\ell\phi)$ (ℓ and ϕ represent the topological charge and azimuthal angle, respectively), it has impelled widespread research interests ranging from optical tweezers[16] and super-resolution imaging[17] to lasers[18]. In addition to these established

application realms, the inherent orthogonality of OAM with theoretically unbounded states carried by OAM beams provides unprecedented new prospects for optical information multiplexing with high capacity and throughput. The success of OAM-multiplexed classical[19-22] and quantum[23] communications compatible with paraxial free-space bulky optics has further strengthened the effectiveness of harnessing OAM division as an independent and versatile dimension to increase the degrees of freedom for information multiplexing. When OAM beams are incorporated with nanophotonics centralized on exploring subwavelength-scale light–matter interactions, mismatch between the typical size of nanostructures and helical wavefront hampers the explicit OAM response at the nanoscale[22]. In addition to OAM, light can also carry spin angular momentum (SAM) associated with circular polarizations. In general, SAM and OAM become strongly coupled in non-paraxial nanophotonic cases[24], where SAM-induced OAM and OAM-induced SAM have recently attracted intense research interests. Essentially, non-paraxial vectorial electric field structures can exhibit complex and versatile local polarization ellipses with variant inclination angles. Such an unheeded degree of freedom—often overlooked for light–matter interactions in the past—might enable nanoscale OAM sensitivity and facilitate nanophotonic information multiplexing[24-30] harnessing the OAM division.

The proposed concept of high-dimensional multiplexing of the OAM of light at the nanoscale is illustrated in Fig. 1. Under tight focusing of a linearly polarized OAM beam (Fig. 1a), the superposition of longitudinal and transverse field components with the associated Gouy phase shifts leads to tilted polarization ellipse distributions within the focal volume (Fig. 1b,c and Supplementary Figs. 1–4). The orientation of local polarization ellipses at a given spatial position within the focus is determined by both OAM-dependent relative amplitudes and Gouy phase differences between the longitudinal and transverse electric field components[31,32]. Tightly focused linearly polarized OAM beams with different topological charges result in distinct polarization ellipses at the same position within the focal spot, which are termed OAM-dependent polarization ellipses here (Supplementary Fig. 2). The disparate rotation of local polarization ellipses (Supplementary Fig. 3) provides a physical mechanism for the selective excitation of nanoparticles by beams of different topological charges. When such focused OAM beams engage with an achiral nanoparticle away from

Fig. 1 | OAM-dependent polarization ellipse-mediated synthetic HD for six-dimensional optical encoding. a, Schematic of a tightly focused linearly polarized OAM beam. The zoomed-in images show that distinct rotations of local polarization ellipses at a given X–Z plane are introduced by focused OAM beams with opposite topological charges $\ell = \pm 1$. **b,c**, Corresponding distributions of polarization ellipses at the Y–Z (**b**) and X–Z (**c**) planes. **d**, Calculated distribution of the electric field amplitude of a plasmonic nanorod, whose geometry centre is located at $Y = 280$ nm and $X = Z = 0$ nm, and the orientation is determined by $\varphi = 45°$, $\theta = 60°$ and excited by tightly focused OAM beams with $\ell = \pm 1$. **e,f**, Linear optical absorption (**e**) and corresponding HD (**f**) of the nanoparticle. **g**, Dependence of HD on the orientation angle of the nanoparticle. In the simulation, the wavelength of the OAM beam is 800 nm, and the numerical aperture (NA) and magnification of the objective lens are 1.4 and ×100, respectively. **h,i**, Schematic of the OAM-based six-dimensional encoding (**h**) and decoding (**i**) of nanometric QR codes utilizing the combinations of four OAM states (helical phase fronts), two polarizations (P_1 and P_2; blue double arrows), and two wavelengths (λ_1 and λ_2) of light and three spatial dimensions in disordered coupling nanoparticle aggregates.

the focal centre, where a randomly aligned gold nanorod (GNR) with a longitudinal surface plasmon resonance (SPR)-mediated dipolar response is considered here (Fig. 1d), the OAM-sensitive orientation of the polarization ellipse at the location of the GNR overwhelmingly determines the excitation strength with respect to different topological charges.

As a result of the non-trivial difference in excitation strengths, synthetic helical dichroism (HD) (Supplementary Note 1) spontaneously emerges in which the GNR exhibits different linear absorptions for OAM beams with opposite topological charges (Fig. 1d–f), enabling an explicit OAM response at the nanoscale. The relative alignment of such a GNR to different local polarization ellipses induced by opposite topological charges can certainly influence the HD strength (Fig. 1g and Supplementary Fig. 4). Unlike conventional HD in chiral structures[33,34], synthetic HD is not restricted to opposite topological charges but, in general, to OAM states with different absolute values of topological charge (Supplementary Fig. 5 and Supplementary Note 1).

However, the HD strength in such an isolated single nanoparticle is too small to be perceivable owing to scale mismatch between the nanoparticles and the diffraction-limited helical wavefronts (Supplementary Note 2). By applying a focused OAM beam to self-assembled nanoaggregates composed of 3D disorderly aligned GNRs, the presence of plasmonic coupling can introduce hotspots with remarkably augmented local fields, which can be adopted to resonantly enhance the synthetic HD (discussed later). Once the power of OAM beams exceeds a thermal reshaping threshold of the GNRs, the enormously amplified HD allows the selective excitation and deformation of different populations of GNRs within the focus of OAM beams with different topological charges, providing a mechanism for nanoscale OAM encoding (Methods and Supplementary Note 3). Moreover, the disordered nature of the self-assembled nanoaggregates automatically endows such HD with simultaneous polarization and wavelength sensitivities for high-dimensional encoding. Leveraging this appealing high-dimensional, sensitive, tightly focused exemplary OAM beams of four different OAM states
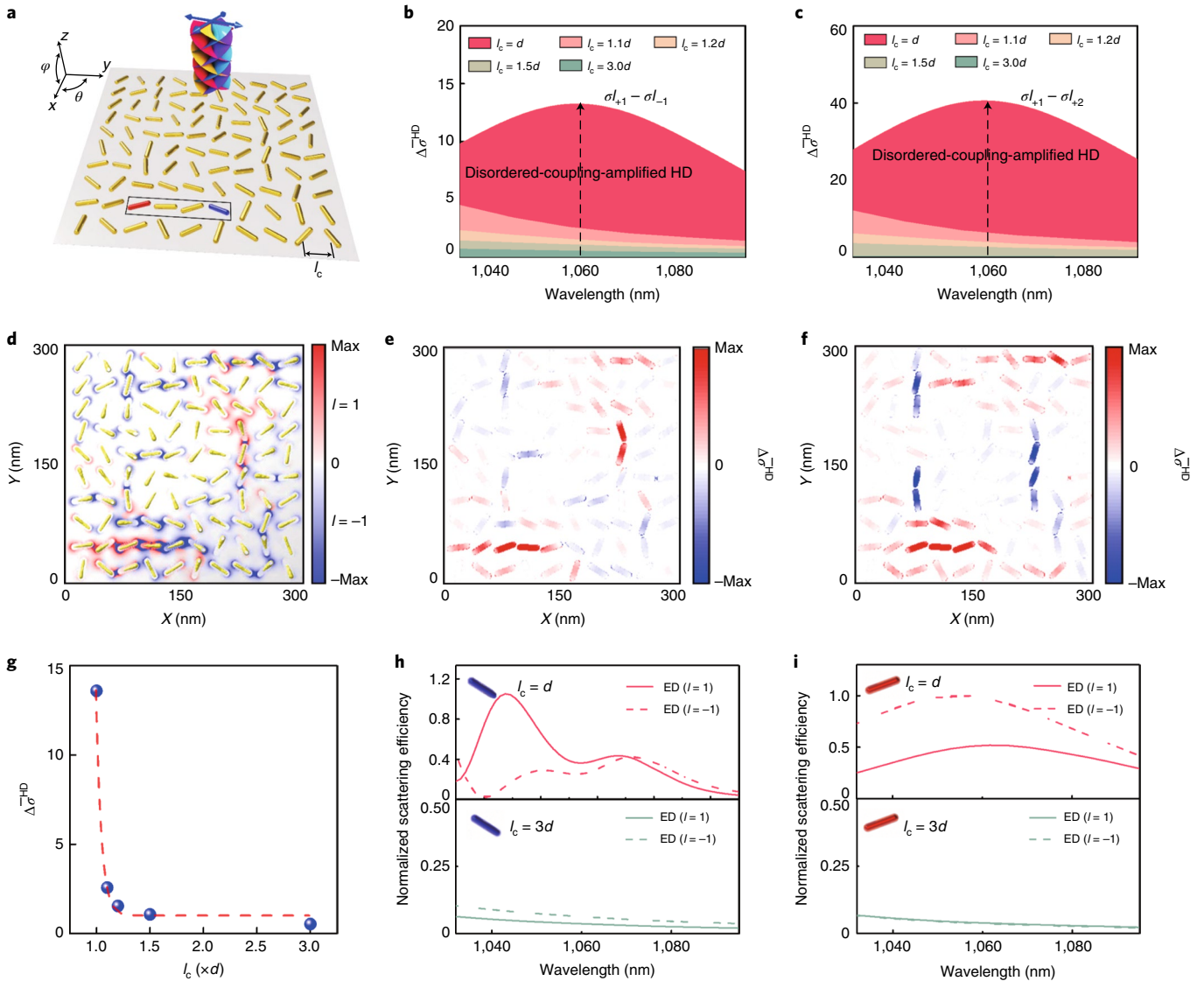
Fig. 2 | Amplified synthetic HD in disordered plasmonic nanoaggregates. a, Simplified model composed of 10×10 randomly oriented GNRs whose centres are arranged in a square lattice with lattice constant l_c normalized to length d of the GNRs. The diameter and length of the GNRs are 8 and 30 nm, respectively, similar to those of the GNRs used in the experiment. Here φ and θ indicate the distributed angles of the GNRs referring to the X and Z axes, respectively. **b,c**, Dependencies of the synthetic HD of the four typical GNRs (marked by the rectangle in **a**) on the lattice constant l_c of the array. $\ell = \pm 1$ is used for **b**, while $\ell = 1$ and 2 are used for **c**. Polarization is fixed linear to the X axis for both cases. The orientations of all the GNRs are fixed when the lattice constant is scaled. **d**, Distribution of electric field intensity $|E|^2$ at the centre plane of the array when the synthetic HD in **b** is maximized, where the red (blue) colour indicates the case of $\ell = 1$ ($\ell = -1$). **e,f**, Difference in electric field intensity ($|E|^2$) inside the GNRs when the synthetic HD in **b** (**e**) and **c** (**f**) is maximized. **g**, Dependence of synthetic HD, integrated over the spectrum range shown in **b** and **c**, on the lattice constant l_c of the array. **h,i**, Electromagnetic multipolar decomposition results for the specified GNRs marked blue (**h**) and red (**i**) in **a**. We only show the results of the ED moment induced in the GNR, since other multipole moments are confirmed to be negligible. The NA and magnification of the objective lens used in the simulation are 1.4 and ×100, respectively.

($-\ell_1 = \ell$, $\ell_2 = 1$ and $-\ell_3 = \ell_4 = 3$) with distinct combinations of two polarizations (linearly polarized along the X and Y directions) and two wavelengths ($\lambda_1 = 800$ nm and $\lambda_2 = 860$ nm) allow us to encode (Fig. 1h) nanometric quick response (QR) code patterns in high dimensions and decode (Fig. 1i) with high fidelity by OAM beams of the same states.

Since the interaction of a tightly focused OAM beam with strongly coupled disordered plasmonic nanoaggregates is complex and physically non-intuitive, to gain insights into the influence of coupling effects on synthetic HD and sensitivity in other dimensions, we use a simplified model of 10×10 GNRs arranged in a

square lattice (Fig. 2a and Methods), where the length and diameter of all the GNRs are 30 and 8 nm, respectively. The 3D alignments of the GNRs (θ, φ) are randomized to mimic a disordered scenario with a uniform random distribution for both in-plane and out-of-plane orientations. By changing the lattice constant l_c, we can flexibly control the coupling strengths among disordered GNRs to account for the synthetic HD in each constituent GNR. The synthetic HD in the four typical GNRs (marked by a rectangle in Fig. 2a) is resonantly enhanced on increasing the coupling strength (that is, reducing the lattice constant l_c) when the array is excited by tightly focused OAM beams with opposite ($\ell = \pm l$) and

different absolute values ($\ell=l$ and 2) of topological charges (Fig. 2b,c). The electric field intensity $|E|^2$ distributions at the peak wavelength of the synthetic HD show that the disordered coupling effect leads to distinct OAM-dependent near-field hotspots for topological charges of $\ell=-1$ and $\ell=1$, where the augmented local fields enormously amplify the synthetic HD in the constituent GNRs (Fig. 2d). A difference in the electric field intensities inside the constituent GNRs arises, leading to the HD for OAM beams with opposite (Fig. 2e) as well as different absolute values (Fig. 2f) of topological charges. It is clearly revealed that the synthetic HD exponentially increases as the lattice constant l_c decreases to smaller than 1.3-fold the length of the rod (d) (Fig. 2g), indicating the deterministic role played by the disordered coupling strengths in the synthesis. The electromagnetic multipolar decomposition results of the two typical GNRs (marked red and blue in Fig. 2a) further reveal that tightly focused OAM beams with opposite topological charges excite distinct electric dipole (ED) moments in the same GNRs when the GNRs are strongly coupled ($l_c=d$), while the induced ED moments become similar when the coupling strength is weak ($l_c=3d$) (Fig. 2h,i). Other high-order electromagnetic multipole moments of the studied GNRs are negligible in the considered wavelength range.

In experiments, we prepared disordered plasmonic nanoaggregates by self-assembling GNRs in polyvinyl alcohol (PVA) at various concentrations to control the disordered coupling strengths (Methods). As an illustration, when a tightly focused OAM ($\ell=-1$) femtosecond pulse interacts with an exemplary self-assembled nanoaggregate consisting of disordered coupling GNRs (Fig. 3a–c), it will excite OAM-sensitive hotspots in the near field (Fig. 3c and Supplementary Figs. 6 and 7). Leveraging a photothermal reshaping mechanism (Methods and Supplementary Note 3), nearby GNRs exhibiting selective absorption of a specific OAM beam given by the synthetic HD will be heated up and deformed into shorter rods once the power of the OAM beam exceeds the melting threshold (Fig. 3b and Supplementary Fig. 8). The acquired transmission electron microscopy images before (Fig. 3a) and after (Fig. 3b) irradiation by a linearly polarized OAM ($\ell=-1$, $\lambda=800$ nm) beam clearly reveal that GNRs highly excited by such an OAM beam are deformed (marked by circles), which is in good agreement with the simulation (Fig. 3c and Supplementary Fig. 8). It should be noted that the excitation wavelength used here is smaller than the resonant wavelength of the simplified model shown in Fig. 2 because the size of the synthesized GNRs is not uniform[35].

Such amplified HD and associated OAM-selective deformation of GNRs can be used to encode binary information '0' or '1' on nanoaggregates in the focal spot with or without photothermal deformation (Methods and Supplementary Note 3). Two-photon luminescence (TPL) that is biquadratically proportional to the electric field inside the GNRs[35] provides an intuitive indication of the synthetic HD experienced by such individual GNRs and can be adopted for decoding, as long as the power is kept below the deformation threshold (Methods and Supplementary Note 3). Although GNRs in the nanoaggregate form exhibit different HD responses among each other due to strong disorder effects, the TPL signal collected from the focal spot by summing the contributions from all the GNRs (more than 4,000 GNRs per focal voxel) reveals no difference before optical encoding because of the ensemble average effect (Fig. 3e). After optically encoding through the selective deformation of a small population of GNRs by a specific OAM beam ($\ell=-1$), the TPL intensity acquired by the low-power decoding OAM beam ($l=-1$) is reduced, which is referred to '0' (dark fluorescence intensity), compared with that by the opposite topological charge ($l=+1$), which is referred to '1' (bright fluorescence intensity) (Fig. 3e,f), because the OAM-sensitive hotspots are different for different topological charges (Fig. 2d and Supplementary Fig. 6). These results explicitly reveal that a change in HD can be faithfully encoded through the photothermal deformation of a population of GNRs near OAM-sensitive hotspots, which leads to a TPL intensity contrast among different encoding channels (Methods and Supplementary Note 3).

At the same time, TPL proportional to two-photon absorption can support a higher sensitivity even for subtle changes in HD after encoding by OAM beams (Fig. 3e,f and Supplementary Fig. 9). Before the optical encoding process, the GNR nanoaggregates inside a focal volume show negligible differences in TPL, implying no dichroism because of the ensemble average effect even at increased optical density (OD) of GNRs (Fig. 3g–i). In sharp contrast, a remarkable TPL contrast (Fig. 3j) can be unambiguously observed with a low-power X-linearly polarized OAM beam ($\ell=3$, 120 μW) at a wavelength of 860 nm after optical encoding ($\ell=3$, 450 μW). More importantly, the principle of OAM-dependent polarization ellipses and hence synthetic HD can be extended to multiple dimensions since the disordered coupling effect in self-assembled nanoaggregates can lead to hotspots with simultaneous wavelength and polarization sensitivity. When changing the wavelength, topological charge and linear polarization orientation of the incident OAM beams, distinct localized hotspots will be excited in the nanoaggregates (Supplementary Figs. 6 and 7). By sweeping the decoding beam with different OAMs (Fig. 3j), wavelengths (Fig. 3k) and polarizations (Fig. 3l), the TPL contrast can be faithfully preserved with multidimensional responses. Furthermore, the TPL contrast proportional to HD can be amplified by increasing the coupling strength among disordered GNRs via an increase in the OD of the self-assembled nanoaggregates from 5 to 100 (Fig. 3j–l), consistent with the trend outlined by the simplified model (Fig. 2b,c). Such a multidimensional response to linearly polarized OAM beams with distinct combinations of OAM, wavelength and polarization is the basis for the subsequent six-dimensional optical encoding, which could be regarded as an alternative for synthetic dimensions in which multidimensional response associated with OAM is enabled by the disordered coupling effect[36].

Moreover, the sensitivity of photothermal deformation and TPL contrast can be enormously increased through the hotspot-amplified HD for faithfully encoding and decoding information. The simulation reveals that the first eight GNRs exhibiting the strongest field

Fig. 3 | Optical encoding through the photothermal deformation mechanism. a,b, Transmission electron microscopy images of the disordered coupling GNRs on a copper wire before (**a**) and after (**b**) irradiation by femtosecond laser pulses ($\ell=-1$, $\lambda=800$ nm, NA = 0.75 and ×20) with an average power of 1,000 μW and exposure time of 25 ms. It should be noted that we use a dry objective lens with low NA of 0.75 and long working distances to coordinate two imaging systems and facilitate the in situ study of the morphology change in the nanoscale. The OAM beam is linearly polarized as indicated in the inset. **c,** Corresponding simulated electric-field amplitude distribution of the structure shown in **a** under the excitation of the same tightly focused linearly polarized OAM beam used in **b**. The deformed GNRs and OAM-sensitive hotspots are outlined by dashed circles. **d,** Schematic of the optical encoding process. **e,f,** TPL signals before (**e**) and after (**f**) optical encoding under the excitation of tightly focused OAM beams with opposite topological charges ($\ell=\pm1$ and $\lambda=800$ nm). **g–i,** Dichroism of OAM beams with different topological charges ($\ell=|n|$) (**g**), wavelengths (**h**) and polarizations (**i**) measured for GNR nanoaggregates with different ODs. **j–l,** Increasing difference in TPL intensities under the excitation of OAM beams with distinct combinations of topological charges ($\ell=|n|$) (**j**), wavelengths (**k**) and polarizations (**l**). Here an OAM beam with a specific topological charge ($\ell=3$), polarization (horizontal) and wavelength ($\lambda=860$ nm) is used for encoding with an average power of 450 μW and exposure time of 25 ms. The error bars reflect fluctuations in the results of multiple experiments.

enhancement in the simplified disordered array model overwhelmingly contribute more than 35% of linear absorption and 73% of TPL signals (Supplementary Fig. 9). This appealing feature allows

the optical encoding of OAM beams with a specific state to only deform the localized HD originating from the first few highly excited GNRs. Based on an optimized encoding power, the TPL
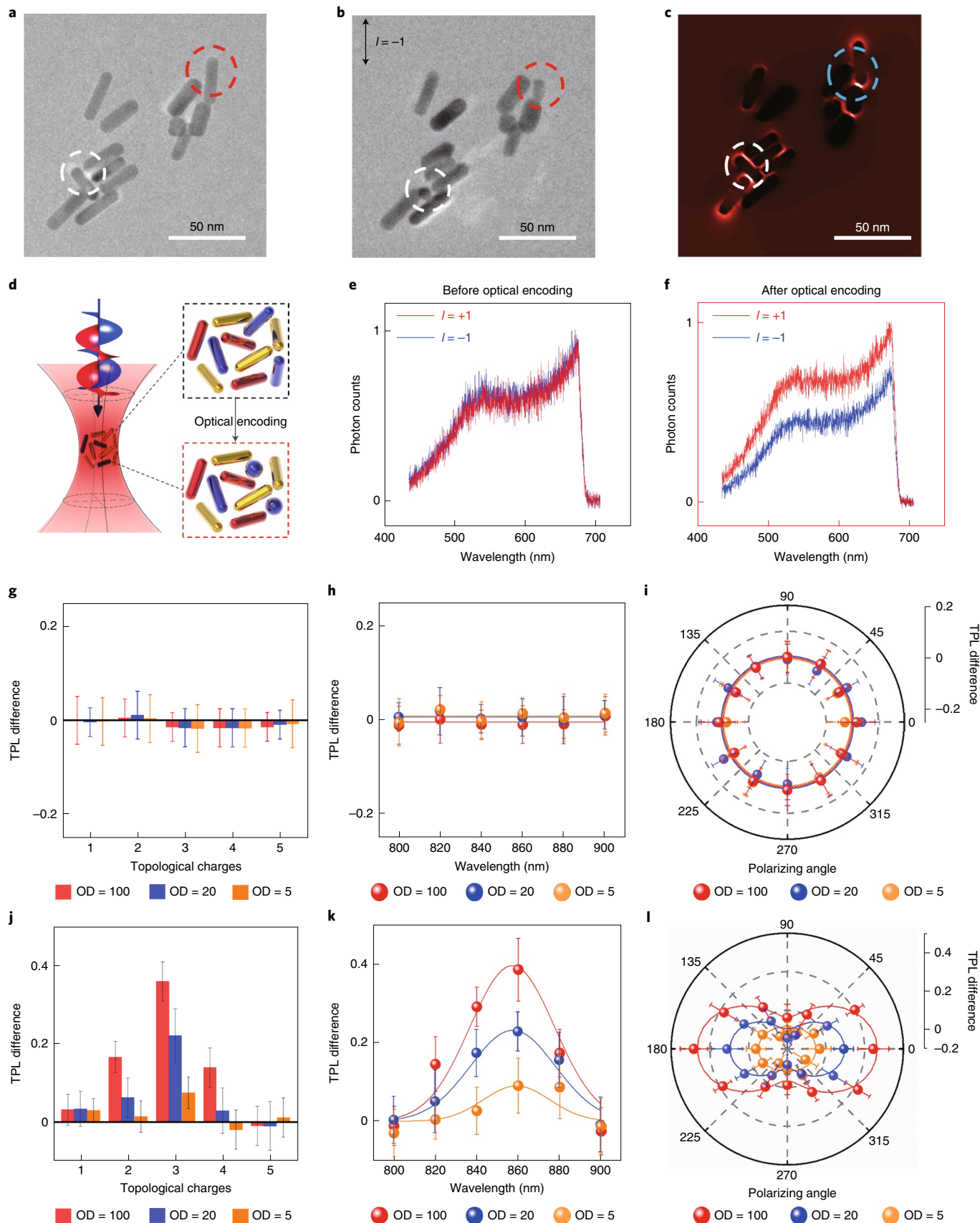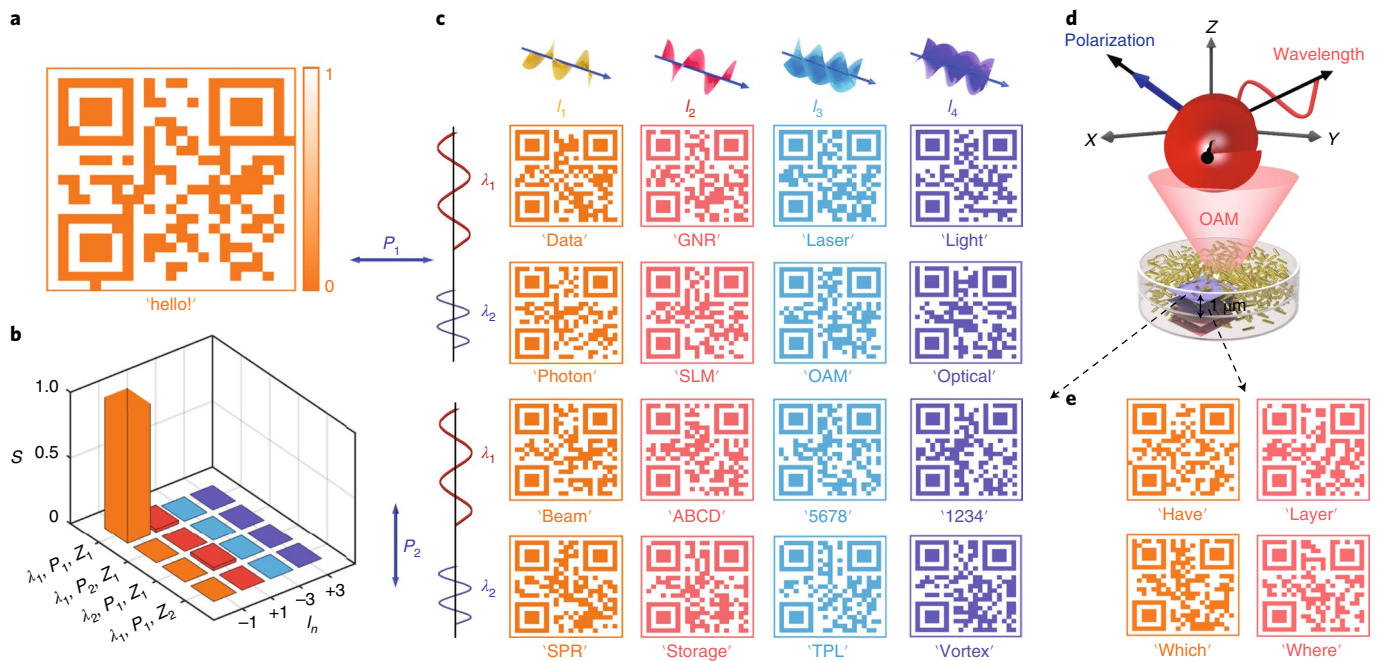
Fig. 4 | Six-dimensional optical encryption and encoding. a, TPL-decoded nanometric QR code encoded in self-assembled GNR nanoaggregates, where the size of the QR code is $32 \times 32\,\mu m^2$ (27×27 multiplexing units). **b**, Similarity factor S evaluating the readout results for OAM beams with other combinations of topological charges, wavelengths, polarizations and Z positions. **c**, Optical multiplexing and demultiplexing of 16 QR codes in the same spatial region. Four OAMs ($-\ell_1 = \ell_2 = 1$ and $-\ell_3 = \ell_4 = 3$), two wavelengths ($\lambda_1 = 800\,nm$ and $\lambda_2 = 860\,nm$) and two linear polarizations are used, as indicated in the insets. An oil-immersion objective lens with NA = 1.4 is employed. **e**, QR codes are multiplexed in the X–Y planes with different Z locations ($Z_1 - Z_2 = 1\,\mu m$); the schematic is shown in **d**. The multiplexing and demultiplexing powers are 250 and $70\,\mu W$ (450 and $120\,\mu W$) for $\ell = \pm 1$ ($\ell = \pm 3$).

signals decoded by OAM beams with different combinations of topological charge, polarization and wavelength from the multiplexing focal volume can then be binarized by using a suitable threshold value to minimize crosstalk among different multiplexing channels (Methods and Supplementary Fig. 10). This type of multiplexing can be repeated in different spatial regions of the disordered medium to cooperate with 3D multiplexing.

In Fig. 4, we demonstrate six-dimensional optical encryption utilizing tightly focused OAM beams. A high NA objective (NA = 1.4) is employed to focus linearly polarized OAM beams at two wavelengths of 800 and 860 nm on the sample containing disordered nanoaggregates with OD = 100 (Supplementary Figs. 11–14). A nanometric QR code composed of 27×27 pixels (the pixel size is approximately $1.2\,\mu m$) was encrypted by a linearly polarized OAM beam ($\ell = -1$) at the wavelength of $\lambda_1 = 800\,nm$ and power of $250\,\mu W$ (Fig. 4a). The similarity factor (Supplementary Note 4) between the target and decoded nanometric QR codes retrieved through TPL by the same OAM beam with a lower power ($\ell = -1$, $70\,\mu W$) can be near unity, while almost crosstalk-free decoding by OAM beams with different topological charges of $\ell = 1$ and ± 3 can be achieved (Fig. 4b and Supplementary Fig. 13). This means that the encrypted QR codes can only be distinctively decoded through the TPL signal excited by the decoding OAM beam with a state identical to that of the encoding beam at the encrypted spatial positions, implying a high level of security. In addition to six-dimensional optical encryption, we demonstrated the encoding of nanometric QR codes in six dimensions, including 3D space (X, Y and Z dimensions), polarization, wavelength and OAM divisions (Fig. 4c–e). Figure 4c depicts sixteen QR patterns retrieved using polychromatic and linearly polarized OAM beams with combinations of four OAM states ($-\ell_1 = \ell_2 = 1$ and $-\ell_3 = \ell_4 = 3$), two wavelengths ($\lambda_1 = 800\,nm$ and $\lambda_2 = 860\,nm$) and two linear polarizations (X and Y polarization) within a specific area ($32 \times 32\,\mu m^2$) in the

X–Y plane. For brevity, only four out of the 16 QR patterns in a parallel X–Y plane $1\,\mu m$ below are shown (Fig. 4d,e; another two layers are shown in Supplementary Fig. 14). The demonstrated nanoscale OAM sensitivity is universal and opens up the possibility for multiplexing OAM beams of physically unbounded states. As one example of multiplexing OAM beams of large absolute values of topological charges, we provide the multiplexing results of $\ell = \pm 5$ and $\ell = \pm 10$ (Supplementary Fig. 15).

Our results unambiguously demonstrate that the multiplexing of OAM beams at the nanoscale in conjunction with the wavelength, polarization and three spatial dimensions can be realized. By tightly focusing OAM beams, the non-paraxial interaction leads to OAM-dependent polarization ellipses in the focus, and hence, a synthetic HD emerged at the nanoscale. This opens new routes for controlling light–matter interactions by harnessing the OAM dimension. In general, the principle of synthetic HD mediated by OAM-dependent polarization ellipses can be extended and generalized to other light–matter interaction systems, which might not only facilitate the study of fundamental science mediated by light's OAM but also underpin tremendous OAM-based applications for high-dimensional quantum entanglement, topological photonics, high capacity information storage, secure encryption and beyond.

Online content

Any methods, additional references, Nature Research reporting summaries, source data, extended data, supplementary information, acknowledgements, peer review information; details of author contributions and competing interests; and statements of data and code availability are available at https://doi.org/10.1038/s41566-021-00880-1.

References

1. Cumpston, B. H. et al. Two-photon polymerization initiators for three-dimensional optical data storage and microfabrication. *Nature* **398**, 51–54 (1999).
2. Richardson, D. J., Fini, J. M. & Nelson, L. E. Space-division multiplexing in optical fibres. *Nat. Photon.* **7**, 354–362 (2013).
3. Zijlstra, P., Chon, J. W. M. & Gu, M. Five-dimensional optical recording mediated by surface plasmons in gold nanorods. *Nature* **459**, 410–413 (2009).
4. Li, X., Lan, T. H., Tien, C. H. & Gu, M. Three-dimensional orientation-unlimited polarization encryption by a single optically configured vectorial beam. *Nat. Commun.* **3**, 998 (2012).
5. Xian, M. et al. Segmented cylindrical vector beams for massively-encoded optical data storage. *Sci. Bull.* **65**, 2072–2079 (2020).
6. Karl, N. J., Mckinney, R. W., Monnai, Y., Mendis, R. & Mittleman, D. M. Frequency-division multiplexing in the terahertz range using a leaky-wave antenna. *Nat. Photon.* **9**, 717–720 (2015).
7. Li, X. et al. Athermally photoreduced graphene oxides for three-dimensional holographic images. *Nat. Commun.* **6**, 6984 (2015).
8. Yun, H., Lee, S. Y., Hong, K., Yeom, J. & Lee, B. Plasmonic cavity-apertures as dynamic pixels for the simultaneous control of colour and intensity. *Nat. Commun.* **6**, 7133 (2015).
9. Dai, Q. et al. Encoding random hot spots of a volume gold nanorod assembly for ultralow energy memory. *Adv. Mater.* **29**, 1701918 (2017).
10. Lu, Y. et al. Tunable lifetime multiplexing using luminescent nanocrystals. *Nat. Photon.* **8**, 32–36 (2014).
11. Fan, Y. et al. Lifetime-engineered NIR-II nanoparticles unlock multiplexed in vivo imaging. *Nat. Nanotech.* **13**, 941–946 (2018).
12. Tan, S. et al. Plasmonic coupling at a metal/semiconductor interface. *Nat. Photon.* **11**, 806–812 (2017).
13. Darwin, C. G. Notes on the theory of radiation. *Proc. R. Soc. Lond. A* **136**, 36–52 (1932).
14. Bazhenov, V. Y., Vasnetsov, M. V. & Soskin, M. S. Laser beams with screw dislocations in their wavefonts. *JETP Lett.* **52**, 429–431 (1990).
15. Allen, L., Beijersbergen, M. W., Spreeuw, R. J. C. & Woerdman, J. P. Orbital angular momentum of light and the transformation of Laguerre-Gaussian laser modes. *Phys. Rev. A* **45**, 8185–8189 (1992).
16. He, H., Friese, M. E. J., Heckenberg, N. R. & Rubinsztein-Dunlop, H. Direct observation of transfer of angular momentum to absorptive particles from a laser beam with a phase singularity. *Phys. Rev. Lett.* **75**, 826–829 (1995).
17. Hell, S. W. & Wichmann, J. Breaking the diffraction resolution limit by stimulated emission: stimulated-emission-depletion fluorescence microscopy. *Opt. Lett.* **19**, 780–782 (1994).
18. Naidoo, D. et al. Controlled generation of higher-order Poincaré sphere beams from a laser. *Nat. Photon.* **10**, 327–332 (2016).
19. Wang, J. et al. Terabit free-space data transmission employing orbital angular momentum multiplexing. *Nat. Photon.* **6**, 488–496 (2012).
20. Bozinovic, N. et al. Terabit-scale orbital angular momentum mode division multiplexing in fibers. *Science* **340**, 1545–1548 (2013).
21. Yan, Y. et al. High-capacity millimetre-wave communications with orbital angular momentum multiplexing. *Nat. Commun.* **5**, 4876 (2014).
22. Fang, X., Ren, H. & Gu, M. Orbital angular momentum holography for high-security encryption. *Nat. Photon.* **14**, 102–108 (2020).
23. Alicia, Sit et al. High-dimensional intracity quantum cryptography with structured photons. *Optica* **4**, 1006–1010 (2017).
24. Bliokh, K. Y., Rodríguez-Fortuño, F. J., Nori, F. & Zayats, A. V. Spin–orbit interactions of light. *Nat. Photon.* **9**, 796–808 (2015).
25. Wong, G. K. L. et al. Excitation of orbital angular momentum resonances in helically twisted photonic crystal fiber. *Science* **337**, 446–449 (2012).
26. Maguid, E. et al. Disorder-induced optical transition from spin Hall to random Rashba effect. *Science* **358**, 1411–1415 (2017).
27. Cai, X. et al. Integrated compact optical vortex beam emitters. *Science* **338**, 363–366 (2012).
28. Miao, P. et al. Orbital angular momentum microlaser. *Science* **353**, 464–467 (2016).
29. Ren, H., Li, X., Zhang, Q. & Gu, M. On-chip noninterference angular momentum multiplexing of broadband light. *Science* **352**, 805–809 (2016).
30. Wang, S. et al. Angular momentum-dependent transmission of circularly polarized vortex beams through a plasmonic coaxial nanoring. *IEEE Photon. J.* **10**, 1–9 (2018).
31. Gouy, L. G. Sur une propriété nouvelle des ondes lumineuses. *C. R. Acad. Sci. Paris* **110**, 1251–1253 (1890).
32. Visser, T. D. & Wolf, E. The origin of the Gouy phase anomaly and its generalization to astigmatic wavefields. *Opt. Commun.* **283**, 3371–3375 (2010).
33. Brullot, W., Vanbel, M. K., Swusten, T. & Verbiest, T. Resolving enantiomers using the optical angular momentum of twisted light. *Sci. Adv.* **2**, e1501349 (2016).
34. Kerber, R. M., Fitzgerald, J. M. & Oh, S. S. Orbital angular momentum dichroism in nanoantennas. *Commun. Phys.* **1**, 87 (2018).
35. Li, J. X. et al. Manipulating light–matter interaction in a gold nanorod assembly by plasmonic coupling. *Laser Photonics Rev.* **10**, 826–834 (2016).
36. Yuan, L., Lin, Q., Xiao, M. & Fan, S. Synnthetic dimension in photonics. *Optica* **5**, 1396–1405 (2018).

Methods

Numerical simulation methods. Vectorial diffraction theory is used to calculate the tightly focused electromagnetic field inside the volume of the focal spot[37]. The OAM beam is linearly polarized. Here the Cartesian electric field components can be calculated by the Richards–Wolf vectorial diffraction theory as follows[37]:

$$E_x(r, \varphi, z) = -\frac{i}{\lambda} \int_0^{2\pi} \int_0^{\alpha} \sin\theta \sqrt{\cos\theta} \, e^{ik[r\sin\theta\cos(\phi-\varphi)+z\cos\theta]}$$
$$\times e^{(il\phi)} \left[\sin^2\phi(1-\cos\theta) + \cos\theta\right] d\phi d\theta, \tag{1}$$

$$E_y(r, \varphi, z) = -\frac{i}{\lambda} \int_0^{2\pi} \int_0^{\alpha} \sin\theta \sqrt{\cos\theta} \, e^{ik[r\sin\theta\cos(\phi-\varphi)+z\cos\theta]}$$
$$\times e^{(i\ell\phi)} \left[\cos\phi\sin\phi(\cos\theta - 1)\right] d\phi d\theta, \tag{2}$$

$$E_z(r, \varphi, z) = -\frac{i}{\lambda} \int_0^{2\pi} \int_0^{\alpha} \sin\theta \sqrt{\cos\theta} \, e^{ik[r\sin\theta\cos(\phi-\varphi)+z\cos\theta]}$$
$$\times e^{(i\ell\phi)} \left[-\cos\phi\,\sin\theta\right] d\phi d\theta, \tag{3}$$

where k is the wave vector; $\alpha = \arcsin\left(\frac{NA}{n}\right)$ is the maximum allowed incident angle determined by the NA of the objective lens; n is the refractive index of the medium where the light–matter interaction occurs; and r, φ and z are the cylindrical coordinates of an observation point. Since we use PVA as the volume matrix to support the disordered coupling GNRs, n is set to 1.518. Then, the calculated field components are used as the excitation source in the finite-difference time-domain method to evaluate the interaction between tightly focused OAM beams and disordered coupling GNRs. In the focal voxel, the calculated focused OAM beams following equations (1)–(3) exhibit characteristic OAM-dependent polarization ellipses within the focal volume dependent on their topological charges (Supplementary Figs. 1–4).

Because the exact modelling of the interaction between the disordered coupling nanoaggregates (Fig. 1h) and the tightly focused OAM beam is challenging, we use a simplified disordered model that consists of 100 GNRs arranged in a 10×10 square array with lattice constant l_c to quantitatively study how the disordered coupling effect can be used to enhance the HD of the constituent GNRs. The focused OAM beam normally impinges on the array. All the GNRs are 30 nm in length and 8 nm in width. The spatial orientations of all the GNRs have a uniform random distribution. The electric field distribution within each GNR and optical absorption of the disordered coupling GNRs can be obtained by the finite-difference time-domain method. A non-uniform grid with the smallest grid size of 0.5 nm as well as perfectly matched layer boundary conditions is adopted in the numerical simulations. The linear and nonlinear optical absorptions of each GNR in the array are calculated following the same procedure as in ref. [35].

At the same time, the induced electromagnetic multipolar moments in each individual GNR can also be evaluated. The radiation power of the ED moment, magnetic dipole moment, electric quadrupole moment and magnetic quadrupole moment based on the Cartesian multipole decomposition method can be respectively calculated as follows[38]:

$$\sigma_{ED} = \frac{\mu_0 \omega^4}{12\pi c} |\mathbf{P}|^2, \tag{4}$$

$$\sigma_{MD} = \frac{\mu_0 \omega^4}{12\pi c} |\mathbf{M}|^2 \tag{5}$$

$$\sigma_{Q^E} = \frac{\mu_0 \omega^4 k^2}{40\pi c} \sum_{\alpha,\beta} \left|\mathbf{Q}_{\alpha,\beta}^E\right|^2, \tag{6}$$

$$\sigma_{Q^M} = \frac{\mu_0 \omega^4 k^2}{160\pi c} \sum_{\alpha,\beta} \left|\mathbf{Q}_{\alpha,\beta}^M\right|^2, \tag{7}$$

where

$$P_\alpha = \frac{1}{i\omega} \int d^3 r J_\alpha(\mathbf{r}),$$

$$M_\alpha = \frac{1}{2c} \int d^3 r \left[r \times J(\mathbf{r})\right]_\alpha,$$

$$Q_{\alpha,\beta}^E = \frac{1}{2i\omega} \int d^3 r \left[r_\alpha J_\beta(\mathbf{r}) + r_\beta J_\alpha(\mathbf{r}) - \frac{2}{3}\delta_{\alpha,\beta}(\mathbf{r} \cdot \mathbf{J}(\mathbf{r}))\right],$$

$$Q_{\alpha,\beta}^M = \frac{1}{3c} \int d^3 r \left[(\mathbf{r} \times \mathbf{J}(\mathbf{r}))_\alpha \mathbf{r}_\beta + (\mathbf{r} \times \mathbf{J}(\mathbf{r}))_\beta r_\alpha\right],$$

μ_0 is the permeability of vacuum, ω is the angular frequency, c is the speed of light in a vacuum and $\mathbf{r}$ specifies the location where the induced current $\mathbf{J}(\mathbf{r})$ is evaluated. Also, $\alpha, \beta = x, y, z$.

Experimental methods. Fabrication of the disordered coupling plasmonic nanoaggregates: GNRs with an average length of ~30 nm and average diameter of ~8 nm are synthesized by using a modified seedless method. The GNR solution is centrifuged first. The speed of the centrifuge is set to 14,000 r.p.m. for 10 min. When centrifugation is completed, the supernatant is removed from the centrifuge tube to obtain the GNR precipitate. Then, we mix 5 μl of the GNR precipitate with 2 ml of ultrapure water, and the absorption spectrum of the mixture is measured by an ultraviolet spectrophotometer. The OD value of the original GNR precipitate can be obtained by multiplying the maximum value of the absorption peak by the dilution factor. Finally, the GNR–PVA mixture is obtained by mixing the GNR precipitate with 8 wt% PVA in different volume ratios to obtain the target OD value of the GNR–PVA mixture. In the six-dimensional optical encryption and multiplexing experiments, the OD value is set to 100.

Optical setup: the optical setup is shown in Supplementary Fig. 11. A femtosecond laser pulse from a Ti:sapphire oscillator (Chameleon, Coherent) with a duration of 140 fs and tuneable wavelength ranging from 680 to 1,080 nm is collimated and expanded by a telescope system. The combination of a half-wave plate and linear polarizer can change the output energy of the laser. The linearly polarized beam is modulated by a spatial light modulator (PLUTO-2-NIR-011, HOLOEYE) to generate the OAM-carrying beam, whose topological charges can be confirmed by the interference results with a collimated beam (Supplementary Fig. 12). Then, the OAM beam with a specific combination of topological charge, polarization and wavelength is redirected by a dichroic beamsplitter (FF720-SDi01-25×36, Semrock) and focused by an objective lens (UPLSAPO 100XO, Olympus) after passing through a 4f system, the f represent focal length. A half-wave plate is used to adjust the laser polarization in the 4f system, and a shutter synchronously coordinated by a computer can control the exposure time when multidimensional light–matter interactions occur. The fluorescence from the sample is collected by the same objective and directed to a fibre-coupled avalanche photodiode (SPCM-AQRH-14-FC, Excelitas Technologies). To confirm the two-photon character of the luminescence, we plot the dependence of the fluorescence intensity on the excitation power on a double-logarithmic scale, in which the slope of the linear fit is 2.12 (Supplementary Fig. 8d). This result confirms the two-photon character of the excitation.

The shutter and 3D stage (P-563.3CD, Physik Instrumente) are synchronously coordinated by homemade software to control the exposure time of the disordered coupling GNRs to the laser. During the optical multiplexing process, the sample is fixed on the 3D stage, and the information is encoded in the disordered medium by moving the 3D stage and opening the shutter. The moving speed of the 3D stage is set to 500 μm s⁻¹, and the exposure time of the shutter is set to 25 ms.

OAM-sensitive light–matter interactions and corresponding encoding and decoding processes: when a tightly focused OAM femtosecond laser interacts with an exemplary disordered coupling GNR nanoaggregate (Fig. 3a), the electric field distributions are distinct for excitations with different topological charges (Supplementary Figs. 6 and 7). During the encoding process, multiple independent bits are encoded in the same spatial region, that is, a voxel of the PVA film consists of disordered coupling GNR nanoaggregates, where the size of the voxel is determined by the focal spot size of the OAM beam. The encoding process involves OAM-sensitive photothermal reshaping, which is essentially a linear optical absorption process. GNRs near the hotspots excited by a tightly focused OAM beam (for example, $\ell = +1$) will heat up to the melting temperature and deform into shorter rods (Fig. 3a–c; another example is provided in Supplementary Fig. 8a–c). As a result, the resonant frequency of the localized surface plasmon for this nanoaggregate system will be altered because of the change in morphology, resulting in a reduction in TPL intensity collected from the same focal spot compared with the non-encoded channel ($\ell = -1$) when the same voxel is excited by a low-power decoding OAM beam (Fig. 3e,f). This means that such a process can be used to record information '0' in the voxel based on the contrast of the decoded TPL intensities among the different channels with and without irradiance by the encoding OAM beams. The non-interacting case corresponds to the encoding of information '1'. It should be noted that information '0' is encoded in such a focal spot with respect to an OAM beam with a specific combination of topological charge, polarization and wavelength[5], which means that multiple independent bits can be encoded and decoded at the same focal spot by OAM beams with distinct combinations of topological charge, polarization and wavelength. When the encoding power is further increased, GNRs might melt by the OAM beams with undesired topological charges, leading to unwanted crosstalk. As a result, a suitable optimum encoding power should be used to minimize crosstalk among the different encoding channels (Supplementary Fig. 10). At the same time, the TPL signals proportional to the nonlinear absorption of GNRs are then digitalized by using a threshold value to minimize crosstalk among the different multiplexing channels (Supplementary Fig. 10). Only a specific combination of topological charge, polarization and wavelength identical to that of the encoding OAM beam can decode the encrypted information.

Data availability

The data that support the plots in this paper and other findings of this study are available from the corresponding authors upon reasonable request.

References

37. Gu, M. *Advanced Optical Imaging Theory* (Springer, 2000).
38. Evlyukhin, A. B., Fischer, T., Reinhardt, C. & Chichkov, B. N. Optical theorem and multipole scattering of light by arbitrarily shaped nanoparticles. *Phys. Rev. B* **94**, 205434 (2016).

Acknowledgements

Author contributions

Competing interests

Additional information